

# Dual Charge-Transfer in Rhenium(I) Thioether Substituted Hexaazanaphthalene Complexes

Holly van der Salm,<sup>†</sup> Michael G. Fraser,<sup>†</sup> Raphael Horvath,<sup>§</sup> Jack O. Turner,<sup>§</sup> Gregory M. Greetham,<sup>||</sup> Ian P. Clark,<sup>||</sup> Michael Towrie,<sup>||</sup> Nigel T. Lucas,<sup>†</sup> Michael W. George,<sup>\*,§,⊥</sup> and Keith C. Gordon<sup>\*,†</sup>

<sup>†</sup>Department of Chemistry and MacDiarmid Institute, University of Otago, Union Place, 9016 Dunedin, New Zealand

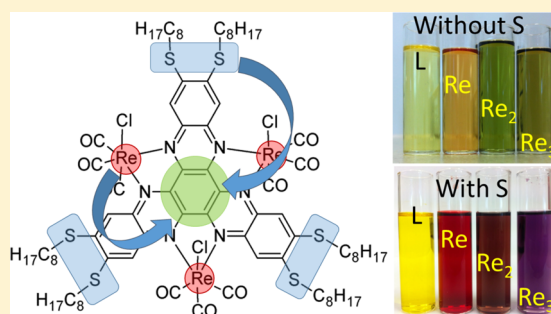
<sup>§</sup>School of Chemistry, University of Nottingham, Nottingham NG7 2RD, United Kingdom

<sup>||</sup>Central Laser Facility, Research Complex at Harwell Science and Technology Facilities Council, Rutherford Appleton Laboratory, Harwell Oxford, Didcot, Oxfordshire OX11 0QX, United Kingdom

<sup>⊥</sup>Department of Chemical and Environmental Engineering, University of Nottingham Ningbo China, 199 Talking East Road, Ningbo 315100, China

## Supporting Information

**ABSTRACT:** The ligand 2,3,8,9,14,15-hexa(octyl-thioether)-5,6,11,12,17,18-hexaazatrinalphthalene (HATN-(SOct)<sub>6</sub>) and its mono-, bi-, and trinuclear Re(CO)<sub>3</sub>Cl complexes are reported. These are characterized by <sup>1</sup>H NMR spectroscopy and electrochemistry, and show broad, intense absorption across the visible wavelength region. Using time-dependent density functional theory (TD-DFT) calculations and resonance Raman spectroscopy these absorption bands are shown to be  $\pi \rightarrow \pi^*$ , MLCT, ILCT(sulfur  $\rightarrow$  HATN), or mixed MLCT/ILCT in nature. Time-resolved infrared spectroscopy is used to probe structural changes and dynamics on short time scales and supports the assignment of a mixed MLCT/ILCT state in which both sulfur groups and one metal center act as electron donors to the HATN core.



## INTRODUCTION

The photophysical properties of rhenium(I) tricarbonyl chloride diimine complexes have been widely studied, as they tend to possess characteristics such as visible absorption, intense emission in solution at room temperature, high <sup>3</sup>MLCT quantum yields, and long-lived excited states which may be oxidizing or reducing in nature.<sup>1–5</sup> Such properties make them useful for photosensitization and photocatalysis, among other things.<sup>6–12</sup> Typical Re(CO)<sub>3</sub>Cl(diimine) complexes, where the diimine is bipyridine- or phenanthroline-based, exhibit <sup>1</sup>MLCT absorptions in the visible (400–500 nm) region and <sup>3</sup>MLCT phosphorescence around 600 nm. These properties may be tuned through appropriate ligand design, which has been shown both experimentally and theoretically.<sup>13</sup>

5,6,11,12,17,18-Hexaazatrinalphthalene (HATN) type ligands have been of interest to researchers due to their ability to act as good electron acceptors and charge carriers.<sup>14,15</sup> In addition, when appended with alkyl chains they self-assemble into discotic liquid crystal phases.<sup>16–18</sup> Recently we reported hexamethyl-substituted HATN (2,3,8,9,14,15-hexamethyl-HATN) and its mono-, bi-, and trinuclear Re(CO)<sub>3</sub>Cl complexes.<sup>19</sup> *Syn* and *anti* isomers, which exist for Re<sub>2</sub> and Re<sub>3</sub> complexes due to axial carbonyl and chloride ligands, were able to be separated by column chromatography. These complexes showed unusual optical properties for Re(CO)<sub>3</sub>Cl-

(diimine) compounds, with low-energy MLCT transitions spanning much of the visible region (400–800 nm).<sup>19</sup>

Previously we have demonstrated that, for a polypyridyl ligand with a low-energy LUMO, attaching electron-rich sulfur-based substituents imbues an intraligand charge transfer (ILCT) from sulfur to polypyridyl.<sup>20,21</sup> This low-energy transition in dipyrro[3,2-*a*:2',3'*c*]phenazine (dppz) substituted with sulfur groups showed an increase in extinction coefficient upon coordination to {Re(CO)<sub>3</sub>Cl}. Resonance Raman spectroscopy and TD-DFT calculations showed this transition to have mixed ILCT(S  $\rightarrow$  dppz)/MLCT(Re  $\rightarrow$  dppz) character.<sup>20</sup>

In this article we present mono-, bi-, and trinuclear {Re(CO)<sub>3</sub>Cl} complexes of a HATN ligand substituted with six octyl-thioether groups (HATN-(SOct)<sub>6</sub>), see Figure 1. These will henceforth be referred to as HATN-S, Re<sub>1</sub>HATN-S, Re<sub>2</sub>HATN-S, and Re<sub>3</sub>HATN-S. The ligand was first published by Kestemont et al., and was shown to form discotic liquid crystals.<sup>16</sup> Electron-rich sulfur groups such as TTF have been attached to the HATN core and show an intense visible ILCT transition.<sup>22,23</sup> The ligand and metal complexes are probed using Raman and resonance Raman spectroscopy, electro-

Received: September 8, 2014

Published: December 3, 2014

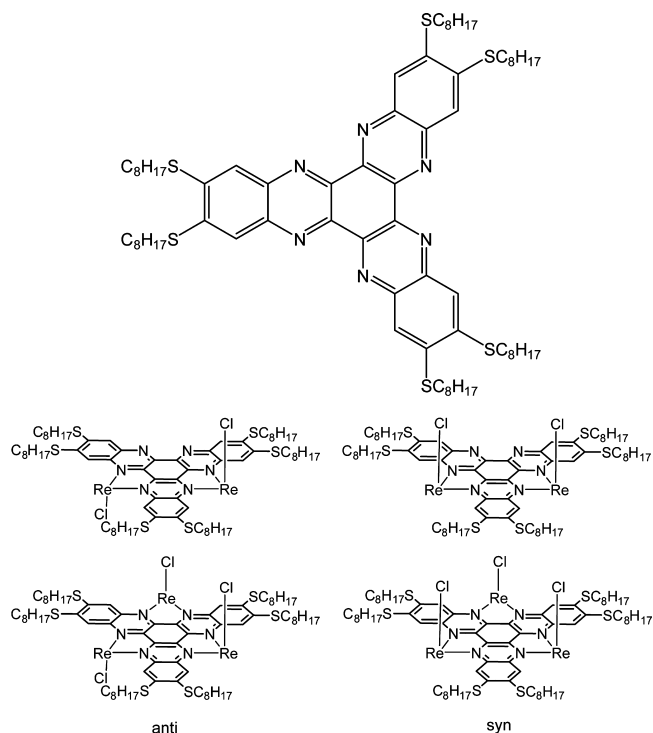


**Figure 1.** Structure of HATN-(SOct)<sub>6</sub> ligand and the *syn* and *anti* isomers of the bi- and trirhenium complexes, where Re represents Re(CO)<sub>3</sub>.

chemistry, electronic absorption with TD-DFT calculations, and time-resolved IR in order to elucidate their electronic behavior.

## RESULTS AND DISCUSSION

**Synthesis and Isomer Separation.** The ligand was synthesized according to literature procedures.<sup>16</sup> The complexes were all produced by refluxing the ligand and Re(CO)<sub>5</sub>Cl with the solvent and stoichiometry used determining the dominant species produced. The complexes were purified, and isomers were separated using column chromatography. Figure 2 shows the <sup>1</sup>H NMR spectra of the compounds in this study. Binding of one {Re(CO)<sub>3</sub>Cl} moiety to the HATN-(SOct)<sub>6</sub> ligand results in three aromatic singlets due to the loss of the D<sub>3h</sub> symmetry of the ligand. Somewhat surprisingly the -CH<sub>2</sub>-S protons are also split, from a triplet in the free ligand at 3.26 ppm (integration 12H), to two multiplets at 3.49 (4H) and 3.28 (8H) ppm, which means they must be close enough to the metal center(s) to be affected. The pattern and integration of the signals for the remaining aliphatic protons resemble that of the free ligand; this is the case for all the complexes studied. Consistent with the {Re(CO)<sub>3</sub>Cl} moiety affecting the CH<sub>2</sub>-S protons, for the *syn* and *anti* isomers of [(Re(CO)<sub>3</sub>Cl)<sub>2</sub>(μ-HATN-(SOct)<sub>6</sub>)], the downfield multiplet (3.50 ppm) has a relative integration of 8H, and the upfield signal (3.30 ppm) of 4H. The two isomers share an aromatic peak at the same chemical shift (8.30 ppm); two of the three peaks assigned to the aromatic protons are at different chemical shifts. The aromatic peak common to both isomers can be assigned as the pair of protons pointing into the uncoordinated pocket of each complex. Without the X-ray crystal structures of the binuclear complexes the assignment of the *syn* and *anti* isomers is achieved through comparing both

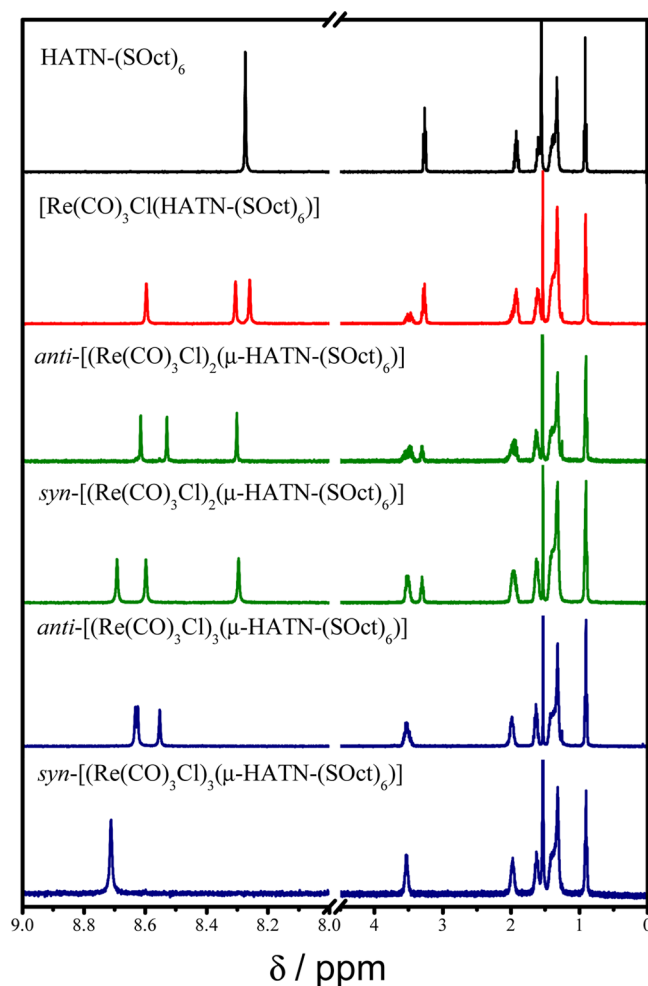


**Figure 2.** Aromatic and aliphatic region of the <sup>1</sup>H NMR (400 MHz, CDCl<sub>3</sub>, 298 K) of the compounds in this study. All spectra are referenced to the residual CDCl<sub>3</sub> peak at 7.26 ppm.

the <sup>1</sup>H NMR chemical shifts and their R<sub>f</sub> values. This is aided by previous knowledge gained from study of the HATN-Me<sub>6</sub> ligand,<sup>15</sup> where assignment is achieved by X-ray crystallography. In both the bi- and trinuclear {Re(CO)<sub>3</sub>Cl} complexes of HATN-Me<sub>6</sub> the respective *anti* isomer has the highest R<sub>f</sub> value. Also, the *syn* isomers in both the methyl and thio-ether binuclear complexes display the largest δ<sup>1</sup>H values.

**Electrochemistry.** The reduction potentials for the HATN-(SOct)<sub>6</sub> ligand and the {(Re(CO)<sub>3</sub>Cl)<sub>x</sub>(μ-HATN-(SOct)<sub>6</sub>)} complexes are shown in Table 1. Irreversible oxidations were observed close to the solvent limit. The reversible first and second reduction potentials are assigned as ligand based

**Table 1.** E<sub>1/2</sub> Values for the First and Second Reduction Processes for HATN-(SOct)<sub>6</sub> and Complexes<sup>a</sup>

compd	E <sub>1</sub> /V	ΔR/V	E <sub>2</sub> /V	ΔR/V
HATN-S	-1.0		-1.2	
Re <sub>1</sub> HATN-S	-0.42	0.58	-0.86	0.34
Re <sub>2</sub> HATN-S	-0.08	0.34	-0.51	0.35
Re <sub>3</sub> HATN-S	0.14	0.22	-0.18	0.33

<sup>a</sup>Calculated as (E<sub>pc</sub> + E<sub>pa</sub>)/2.<sup>24</sup> ΔR is the difference in potential due to the addition of a metal centre, so for Re<sub>2</sub>HATN-S, ΔR = E(Re<sub>2</sub>HATN-S) - E(Re<sub>1</sub>HATN-S).

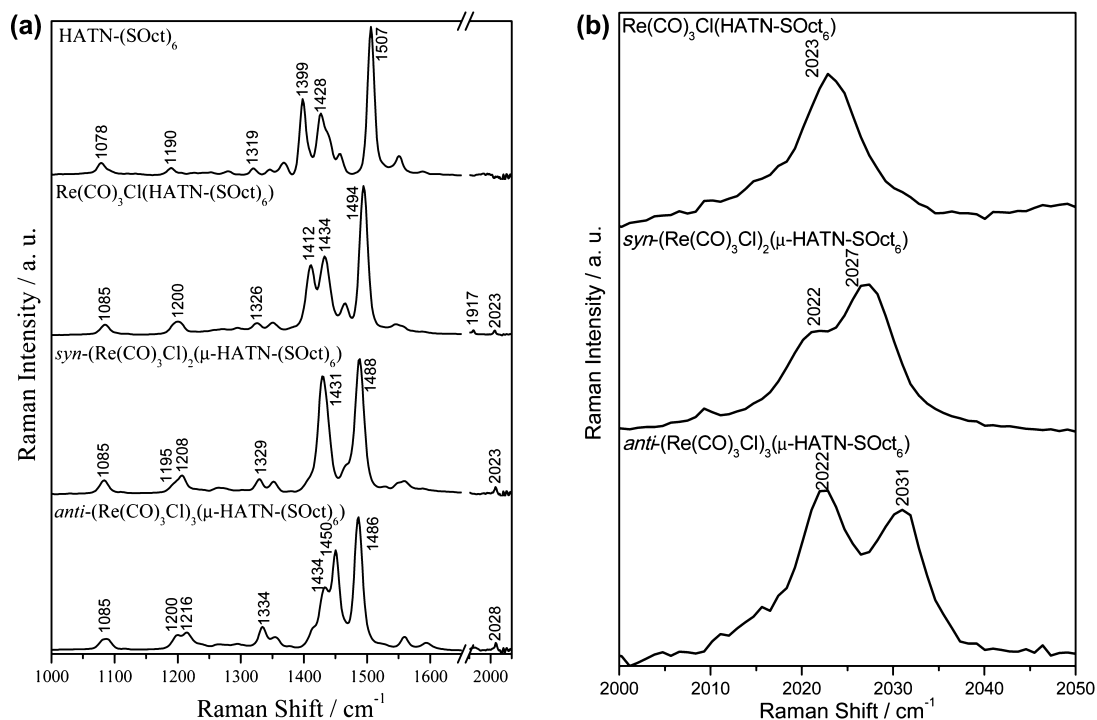


Figure 3. FT and resonance Raman spectra of ligand and complexes.

reductions. The reduction potential for HATN-S is stabilized by almost 600 mV on chelation of a single {Re(CO)<sub>3</sub>Cl} moiety. The binding of a second and third metal center has a diminishing effect, with the reduction potentials stabilized by 340 and 220 mV, respectively. The reduction potentials of the ligand and complexes are very similar to those of the hexamethyl-substituted ligand previously studied.<sup>19</sup> This is consistent with the nature of the LUMOs as calculated by DFT, that show electron density is largely centered on the aromatic core of the ligand.

**FT-Raman Spectroscopy.** FT-Raman spectra were recorded on solid samples, and for both the ligand and complexes spectra are dominated by a few strong bands, see Figure 3. The strongest band in all spectra is assigned to a vibration of the HATN core, and this shifts to lower energy with an increasing number of metal centers, from 1507 cm<sup>-1</sup> for HATN-S, to 1494, 1488, and 1486 cm<sup>-1</sup> for Re<sub>1</sub>HATN-S, Re<sub>2</sub>HATN-S, and Re<sub>3</sub>HATN-S complexes, respectively. Carbonyl bands are not obvious in FT-Raman spectra, but the symmetric stretch is observed when resonantly enhanced due to MLCT excitation, such as at 532 nm, see Figure 3b. This band is split in two when there are multiple {Re(CO)<sub>3</sub>Cl} centers, since the CO groups on each center may be in-phase or out-of-phase with one another.

**Electronic Absorption Spectra, TD-DFT Calculations, and Resonance Raman Spectroscopy.** Electronic absorption spectra of HATN-S and the rhenium complexes are shown in Figure 4, and relevant data are shown in Table 2. As with previous HATN-Me<sub>6</sub><sup>19</sup> compounds, these are intensely colored, and as the number of rhenium centers is increased, solution colors change dramatically. HATN-S and Re<sub>1</sub>HATN-S show two strong peaks almost equal in intensity, at 363 and 479 nm for the ligand and 422 and 548 for Re<sub>1</sub>HATN-S. With an increasing number of rhenium centers, the spectra become broader with less defined peaks. As the spectra of the *syn* and *anti* isomers of Re<sub>2</sub>HATN-S and Re<sub>3</sub>HATN-S are expected to

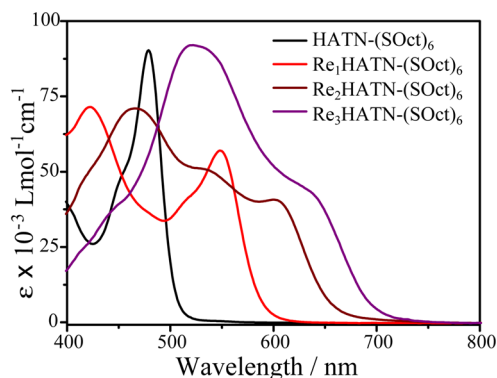


Figure 4. UV-vis absorption spectra of HATN-S (black) and complexes (Re<sub>1</sub>HATN-S = red, Re<sub>2</sub>HATN-S = brown, Re<sub>3</sub>HATN-S = purple) recorded in CH<sub>2</sub>Cl<sub>2</sub>.

be nearly identical, as has previously been shown for the analogous HATN-Me complexes,<sup>19</sup> only one of each is shown.

The HATN-S absorption spectrum shows a similar shape to that of dppz(Sdec)<sub>2</sub>,<sup>20</sup> with some variation in relative peak intensities. B3LYP TD-DFT calculations predict the lowest energy band and shoulder to be an equal donation from the SOct groups to the HATN core, where electron density is accepted equally. There are no marker bands in Raman spectra for ILCT(S → HATN) because the bonds involved are not highly polarizable, especially when compared to the large HATN π system. The higher energy transition (363 nm) is predicted by B3LYP TD-DFT calculations to be π → π\* in nature, which is consistent with resonance Raman spectra recorded at 351, 356, 406, and 413 nm showing resonant enhancement of vibrations of the HATN core (Figure 5a), as this is where the π system resides. CAM-B3LYP TD-DFT calculations, which are used for charge transfer transitions, predict all of the strong transitions for the ligand to be sulfur to HATN ILCT transitions, see Table 3. It is interesting to note

Table 2. Experimental and Calculated B3LYP Electronic Transitions ( $\text{CH}_2\text{Cl}_2$  Solvent Field, IEFPCM Model) of Selected Isomers<sup>a</sup>

		exptl		calcd	
band energy/nm	$\epsilon \times 10^{-3}/\text{L mol}^{-1} \text{ cm}^{-1}$	band assignment	band energy/nm	<i>f</i>	orbital contributions (%)
HATN-S					
479	90.3	S → HATN	457	0.202	H → L (93)
			457	0.203	H - 1 → L (93)
450	46.2	S → HATN	391	0.159	H - 1 → L + 1(41)
					H → L + 2(41)
			391	0.158	H - 1 → L + 1 (42)
					H → L + 1(41)
363	74.1	$\pi \rightarrow \pi^*$	318	0.72	H - 10 → L + 1(10)
					H - 9 → L + 2(10)
					H - 7 → L + 1(37)
					H - 6 → L + 2(37)
			318	0.723	H - 10 → L + 2(10)
					H - 7 → L + 2(37)
					H - 6 → L + 1(36)
Re <sub>1</sub> HATN-S					
548	57.0	MLCT	443	0.269	H - 10 → L(14)
					H - 9 → L(48)
					H - 8 → L + 1(27)
514	40.2	MLCT	441	0.134	H - 10 → L(14)
					H - 9 → L(48)
					H - 8 → L + 1(27)
422	71.5	$\pi \rightarrow \pi^*$	374	0.896	H - 10 → L + 2(33)
					H - 9 → L + 1(18)
					H - 9 → L + 2(11)
388	61.3	$\pi \rightarrow \pi^*$	373	0.338	H - 10 → L + 1(20)
					H - 10 → L + 2(12)
					H - 9 → L + 2(42)
syn-Re <sub>2</sub> HATN-S					
603	40.6	S → HATN	624	0.085	H - 7 → L(26)
					H - 3 → L(52)
538	50.4	MLCT	543	0.055	H - 10 → L(26)
					H - 2 → L + 1(40)
					H - 1 → L + 1(16)
467	71.0	S → HATN	446	0.102	H - 9 → L + 1(18)
					H - 6 → L + 1(12)
					H - 6 → L + 2(53)
418	48.4	MLCT	405	0.108	H - 15 → L(76)
					H - 10 → L + 2(16)
378	27.5	$\pi \rightarrow \pi^*$	356	0.07	H - 23 → L(22)
					H - 22 → L(23)
					H - 21 → L + 1(12)
					H - 20 → L + 1(14)
anti-Re <sub>3</sub> HATN-S					
637	43.1	M + S → HATN	845	0.021	H - 5 → L + 2(34)
					H - 4 → L(44)
522	92.0	M + S → HATN	745	0.238	H - 6 → L(11)
					H - 5 → L + 2(29)
					H - 4 → L + 1(13)
			742	0.249	H - 7 → L(14)
					H - 4 → L + 2(24)
					H - 3 → L + 1(22)

<sup>a</sup>S and M refer to the SOct and {Re(CO)<sub>3</sub>Cl} substituents, respectively.

that both B3LYP and CAM-B3LYP TD-DFT calculations predict two transitions at the same energy and similar oscillator strength for each band.

The nature of transitions predicted for Re<sub>1</sub>HATN-S by B3LYP and CAM-B3LYP TD-DFT calculations is not the

same, although in both cases the two lowest energy transitions are predominantly MLCT, with a greater involvement of the sulfur groups predicted by CAM-B3LYP. Higher energy transitions predicted by B3LYP (374, 373 nm) are  $\pi, \pi^*$  in nature, while CAM-B3LYP predicts MLCT (406 nm), and

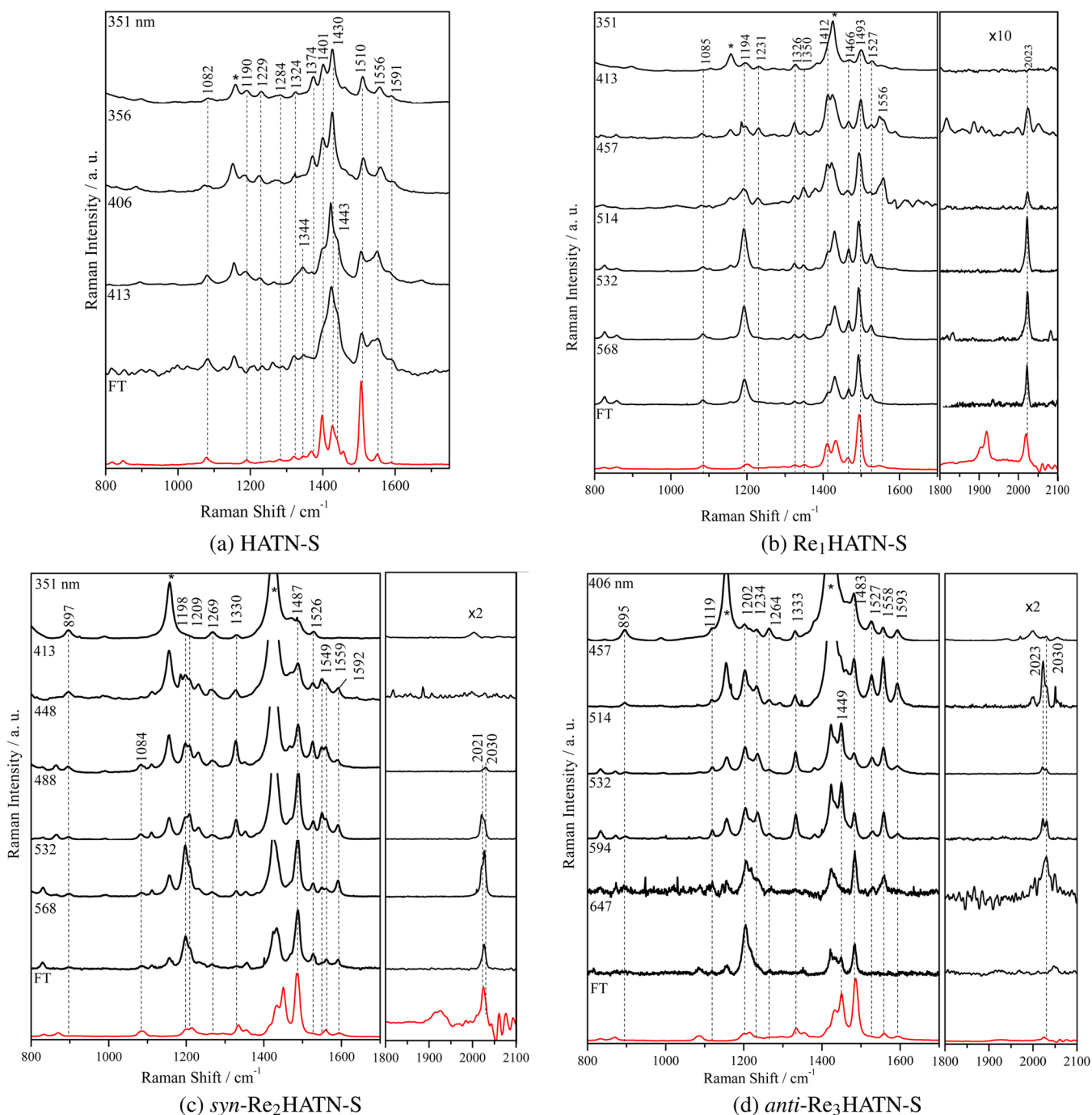


**Figure 5.** Resonance Raman spectra of compounds in  $\text{CH}_2\text{Cl}_2$  at a range of excitation wavelengths. The symbol \* denotes solvent bands. For the complexes, the carbonyl region is amplified by the factor indicated.

metal and sulfur to HATN (380 nm) and ILCT (364 nm); this functional shows bias toward charge transfer states and as such is less likely to predict  $\pi, \pi^*$  type transitions. There is precedence for CAM-B3LYP improving the predicted energy of charge transfer transitions.<sup>25</sup> Resonance Raman spectra recorded from 351 to 568 nm show a change in the pattern of band enhancement (see Figure 5b), although in all spectra the strongest band ( $1495 \text{ cm}^{-1}$ ) is assigned as a vibration of the two HATN arms adjacent to the metal center. At the shortest wavelengths (351, 356 nm), HATN vibrational modes at 1231, 1412, and  $1556 \text{ cm}^{-1}$  show the greatest enhancement, while at longer wavelengths different HATN modes at 824, 1194, and

$1493 \text{ cm}^{-1}$  are enhanced, as is the in-phase symmetric stretch of the CO groups at  $2023 \text{ cm}^{-1}$ , which is indicative of MLCT due to a change in electron density at the metal center. Resonance Raman spectroscopy shows evidence of MLCT at the longest wavelengths, ILCT at intermediate wavelengths, and  $\pi, \pi^*$  at higher energy, which is reasonably consistent with TD-DFT predictions of either functional as to the nature of transitions, although neither agrees completely with experimental evidence.

Addition of a second  $\{\text{Re}(\text{CO})_3\text{Cl}\}$  metal center results in a much broader absorption spectrum. Both B3LYP and CAM-B3LYP TD-DFT calculations predict several transitions with similar oscillator strength, but these differ in energy and nature.

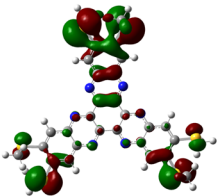
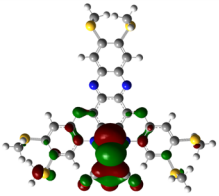
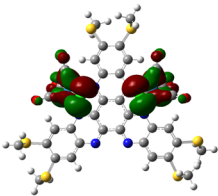
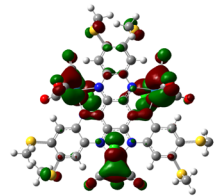
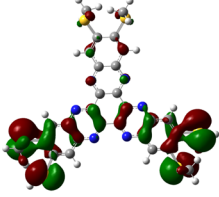
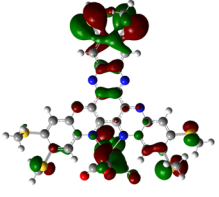
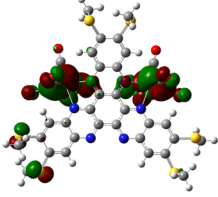
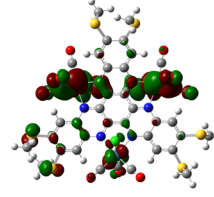
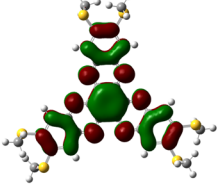
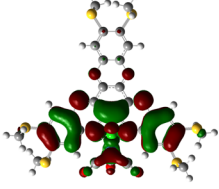
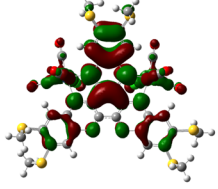
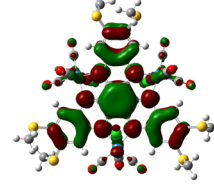
Table 3. Experimental and Calculated CAM-B3LYP Electronic Transitions (CH<sub>2</sub>Cl<sub>2</sub> Solvent Field, IEFPCM Model) of Selected Isomers

exptl		calcd			
band energy/nm	$\epsilon \times 10^{-3}/\text{L mol}^{-1} \text{cm}^{-1}$	band assignment	band energy/nm	<i>f</i>	orbital contributions (%)
HATN-S					
479	90.3	S → HATN	338	0.739	H → L(54)
		S → HATN	338	0.740	H - 1 → L(54)
450	46.2	S → HATN	281	0.361	H → L + 2(11)
		S → HATN	281	0.381	
		S → HATN	280	0.431	H - 13 → L + 1(29)
		S → HATN	280	0.346	H - 13 → L + 2(29)
363	74.1	S → HATN	265	0.409	H - 2 → L + 2(16)
		S → HATN	265	0.418	H - 2 → L + 1(16)
Re <sub>1</sub> HATN-S					
548	57.0	M + S → HATN	490	0.001	H - 1 → L(11)
					H → L(84)
514	40.2	M + S → HATN	448	0.049	H - 2 → L(18)
					H - 1 → L(56)
422	71.5	MLCT	406	0.010	H - 8 → L(74)
388	61.3	S → HATN	380	0.552	H - 3 → L(59)
			364	0.205	H - 6 → L(16)
					H - 4 → L(32)
<i>syn</i> -Re <sub>2</sub> HATN-S					
603	40.6	MLCT	553	0.014	H - 1 → L(26)
					H → L(52)
538	50.4	MLCT	546	0.002	H - 2 → L(56)
					H - 1 → L(23)
467	71.0	M + S → HATN	501	0.101	H - 5 → L(11)
					H - 2 → L(17)
					H - 1 → L(27)
					H → L(30)
418	48.4	S → HATN	411	0.333	H - 6 → L(28)
					H - 3 → L(24)
378	27.5	S → HATN	391	0.155	H - 14 → L(13)
					H - 9 → L(21)
					H - 5 → L(14)
					H - 3 → L + 1(10)
<i>anti</i> -Re <sub>3</sub> HATN-S					
637	43.1	MLCT	593	0.003	H - 2 → L(14)
					H - 1 → L(25)
					H - 1 → L + 2(10)
					H → L(28)
522	92.0	M + S → HATN	522	0.059	H - 4 → L(12)
					H - 3 → L(10)
					H → L(23)
		M + S → HATN	514	0.071	H - 5 → L(11)
					H - 3 → L(12)
					H - 1 → L(12)
					H → L + 2(17)
		S → HATN	432	0.300	H - 6 → L(19)
					H - 3 → L(19)
			427	0.368	H - 7 → L(11)
		M + S → HATN			H → L + 1(25)

With B3LYP TD-DFT, the lowest energy transition (exptl 603 nm, calcd 624 nm) is predicted to be from the SOct groups to HATN. Sulfur donation is not predicted to be completely equal (see Supporting Information Table S1), and the HATN arm between the two metals is predicted to accept a significantly greater amount of electron density than the other two. Higher energy transitions are predicted to have MLCT nature. With CAM-B3LYP, the lowest energy transitions (exptl 603, 538 nm;

calcd 553, 546 nm) are predicted to be MLCT in nature, with higher energy transitions (exptl 418, 378 nm; calcd 411, 391 nm) transitions predicted to be sulfur to HATN ILCT transitions, with intermediate transitions (exptl 467 nm; calcd 501 nm) with mixed sulfur and metal donation. Loss of electron density from the metal center(s) is supported by resonant enhancement of carbonyl bands between 351 and 568 nm (Figure 5c). HATN bands are enhanced in all spectra, with

Table 4. Frontier Molecular Orbitals

MO	HATN-S	Re <sub>1</sub> HATN-S	syn-Re <sub>2</sub> HATN-S	anti-Re <sub>3</sub> HATN-S
H-1				
HOMO				
LUMO				

a pattern similar to that of the single Re complex. The 1330  $\text{cm}^{-1}$  vibrational mode associated with the sulfur substituents is strongly enhanced at 448 and 488 nm, lending some support to the CAM-B3LYP TD-DFT calculations. It is expected that  $\pi \rightarrow \pi^*$  transitions are shifted further to the UV and are not observed or probed here.

Addition of a third metal center results in more interesting transitions that are from both sulfur groups and metals to the HATN core, similar to those observed by Fraser and co-workers<sup>20</sup> for sulfur-dppz systems. TD-DFT calculations with the B3LYP functional predict predominantly sulfur to HATN at 845 nm (exptl 637 nm), but still with some MLCT contribution. Transitions in which both the sulfur groups and the metal donate an approximately equal amount of electron density to the HATN-S ligand are predicted at 745, 742 nm (exptl 522 nm). If the CAM-B3LYP functional is used, the energy of transitions is more reasonable, with MLCT predicted at 593 nm. As with B3LYP, mixed transitions in which both the sulfur and metal donate electron density to the HATN are predicted at higher energy. Resonance Raman spectra are consistent with such assignments (Figure 5d), with a 1333  $\text{cm}^{-1}$  vibration of sulfur groups (see Supporting Information Table S1) showing enhancement from 406 to 532 nm, and carbonyl bands (2023, 2030  $\text{cm}^{-1}$ , these are the in-phase symmetric stretches of CO groups on one metal center, which can be in-phase or out-of-phase between metal centers<sup>19</sup>) showing enhancement from 532 to 594 nm. Other changes in the profile of bands relate to HATN vibrations, and therefore are not informative as to the nature of the transitions because the HATN always acts as the acceptor moiety.

Because sulfur and/or metal to HATN transitions are charge transfer in nature, it is expected that CAM-B3LYP TD-DFT calculations should be more accurate than B3LYP.<sup>26–28</sup> However, in some cases B3LYP appears to show better agreement with experimental resonance Raman data with regard to the nature of transitions.

The FMOs are shown in Table 4; these do not describe all of the transitions but are significant in many.

Because both the sulfur groups and the metals can act as donors to the HATN, it is of interest to probe the individual sulfur and metal donors in greater detail. To do this, the molecules were divided into their components, and Mulliken charge analysis applied. Partitioning of the molecules is shown in Figure 6, where in complexes with fewer than three metal centers, the relevant color is not present in the table, see Supporting Information Tables S1 and S2.

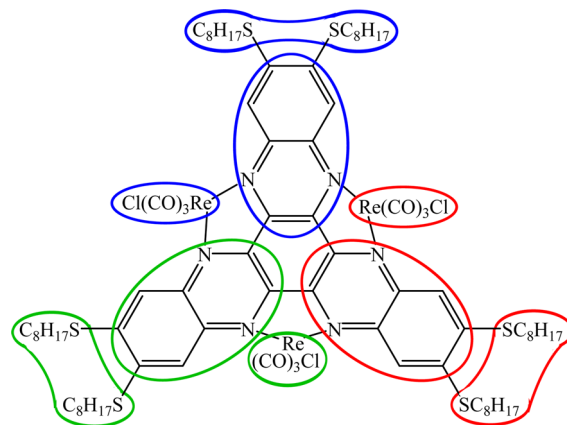
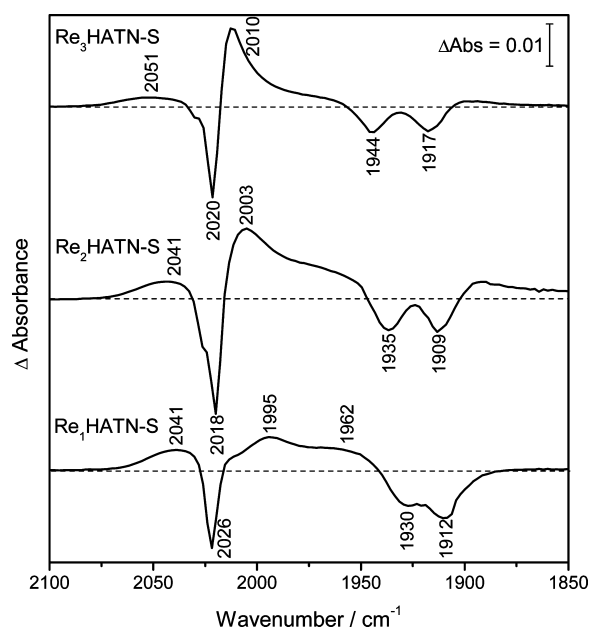


Figure 6. Grouping of molecular components used in Mulliken analysis of charge transfer.

In the ligand sulfur to HATN transitions, all of the sulfur groups are predicted to donate electron density equally, in both B3LYP and CAM-B3LYP calculations, and each HATN “arm” is predicted to accept electron density equally, because the ligand is highly symmetric. Inclusion of one metal center adds an extra possible donor, and reduces the symmetry. Here, the lower energy MLCT to HATN transitions are predicted to terminate on the two HATN arms adjacent to the metal center, which seems logical as these arms have one nitrogen chelated to the metal each, while the third has neither nitrogen bound.

When the second metal is added, transitions become more complicated. B3LYP TD-DFT calculations predict ILCT as the lowest energy transition (exptl 603 nm; calcd 624 nm), while MLCT is predicted by CAM-B3LYP (exptl 603, 538 nm; calcd 553, 546 nm). Nonetheless, in both cases the HATN arms between the two metal centers accept significantly more electron density than the other two, as it is the most electron deficient. There are less clear trends for the other transitions, see Supporting Information Tables S1 and S2. In *anti*-Re<sub>3</sub>HATN-S, the Re center which is *anti* donates more electron density than the other two. Sulfur groups donate relatively equally in all transitions, as these are in very similar environments and may not be affected by the configuration at the closest metals.

**Time-Resolved Infrared Spectroscopy.** The TRIR spectra of the HATN-S complexes after excitation at 400 nm are shown in Figure 7, and kinetics of major features are in



**Figure 7.** TRIR spectra of the HATN-S complexes in CH<sub>2</sub>Cl<sub>2</sub>, 100 ps after photolysis with a 400 nm pulse.

Figure 8. The exact lifetimes and the peak positions are summarized in Table 5. As the *syn* and *anti* complexes show near-identical features, only the former are included. TRIR spectroscopy is a powerful probe of excited states of coordination compounds, particularly using the frequency shifts ( $\Delta\nu$ ) of reporter groups, such as CO.<sup>29</sup> A change in vibrational frequency of the  $\nu(\text{CO})$  bands is caused by a change in back-bonding into the carbonyl antibonding orbitals by a partial oxidation of the excited state metal center or by a reduced ligand. The direction and magnitude of  $\Delta\nu$  can then be related to the type of excited state formed. As mentioned, we have previously reported the use of TRIR to unravel the nature and reactivity of related compounds containing HATN-Me.<sup>19</sup> The precise identities of the vibrational  $\nu(\text{CO})$  bands have been assigned with reference to elegant 2D-IR work by Hamm and co-workers on [Re(CO)<sub>3</sub>Cl(bpy)].<sup>30</sup>

The TRIR spectra of Re<sub>1</sub>HATN-S show depletion of the parent bands at 1912, 1930, and 2026 cm<sup>-1</sup>, concurrent with the appearance of a reasonably intense and broad band centered at 1968 cm<sup>-1</sup> and a smaller band at 2035 cm<sup>-1</sup> at early

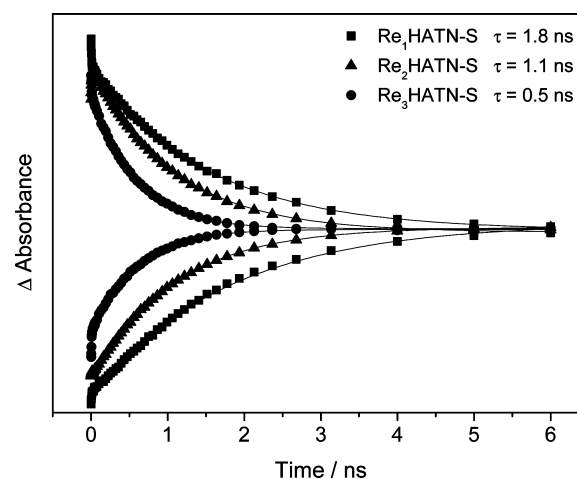


**Figure 8.** Decays of the  $a'(1)$  feature and recovery of the corresponding parent depletion for all complexes. Early times are affected by vibrational cooling.

times. These bands blue-shift rapidly (6 ps) to reveal peaks at 1962, 1995, and 2041 cm<sup>-1</sup> (see Figure 7), and this process is assigned to vibrational cooling, with reference to data presented for the bimetallic and trimetallic complexes below. These bands decay to reform the ground state with a lifetime of 1.8 ns (Figure 8). The shift of  $\Delta\nu$  to higher energies is consistent with a metal to ligand charge transfer state as assigned previously for analogous complexes containing HATN.<sup>19</sup> The shift of the Re<sub>1</sub>HATN-S complex is 15 cm<sup>-1</sup>, compared to 33 cm<sup>-1</sup> for the analogous Re<sub>1</sub>HATN complex, implying that the metal center is significantly less oxidized in the excited state of the sulfur-containing complex. This could be due to either an inductive effect of the sulfur substituents or a different type of excited state, whereby the metal and sulfur moieties both act as electron donors, each contributing electron density. Precedence for such a state has been found for sulfur-substituted dppz complexes.<sup>20</sup> The Re<sub>2</sub>HATN-S and Re<sub>3</sub>HATN-S complexes show depletion of the parent bands at the earliest time delays and, similarly to the Re<sub>1</sub>HATN-S complex, appearance of broad and intense features. Again, these sharpen and blue-shift over the course of several picoseconds to reveal final band positions that are consistent with MLCT excited states. Important differences with respect to the Re<sub>1</sub>HATN-S complex exist. First, in addition to the bands due to the photoexcited metal centers further bands are observed slightly red-shifted with respect to the parents that are due to the “unoxidized” spectator metal centers. This is indicative of localization of the excited state on the time scale of the experiment. Second, the magnitude of the shift in  $\nu(\text{CO})$  bands on going from the ground to the MLCT excited state values is greater. This is most clearly seen by comparing the high frequency  $a'(1)$  stretch of Re<sub>2</sub>HATN-S and Re<sub>3</sub>HATN-S complexes which shift by 22 and 30 cm<sup>-1</sup>, respectively. This is indicative of the electron-withdrawing effects of rhenium metal centers, which delocalize the excited-state electron across the HATN-S disk, leading to a stabilization of the excited state.<sup>20</sup> Similarly, the peaks due to spectator metal centers appear closer to the parent depletions for the trimetallic complex. This delocalization of the excited state is consistent with the calculated LUMOs (*vide supra*), which become progressively more delocalized as the number of metals increases; it is reasonable to assume the same trend holds for the singly occupied orbitals of the excited states, which is



Table 5. Summary of the Vibrational Peak Positions and Lifetimes<sup>a</sup>

compd	$\nu(\text{CO})/\text{cm}^{-1}$	$\nu(\text{fingerprint})/\text{cm}^{-1}$	lifetime/ns	assignment
Re <sub>1</sub> HATN-S	1877, 1890		0.35	$\pi,\pi^b$
	1962, 1995, 2041 <sup>b</sup>	1376, 1410, 1476, 1497, 1527, 1582	0.007, <sup>c</sup> 1.8	MLCT
	1912, 1930, 2026	1348, 1415, 1429, 1461		GS
Re <sub>2</sub> HATN-S	1892, <sup>d</sup> 1968, 2003, <sup>d</sup> 2041	1343, 1375, 1397, 1461, 1478, 1512, 1536, 1579	0.006, <sup>c</sup> 1.1	MLCT
	1909, 1935, 2018, 2024 <sup>c</sup>	1351, 1415, 1431, 1466		GS
Re <sub>3</sub> HATN-S	1896, <sup>d</sup> 1977, 2010, <sup>d</sup> 2051	1385, 1400, 1454, 1478, 1502, 1511, 1538, 1579	0.007, <sup>c</sup> 0.5	MLCT
	1917, 1944, 2020, 2028 <sup>e</sup>	1356, 1415, 1433, 1558		GS

<sup>a</sup>Excited and ground state (GS) data are from TRIR and FTIR techniques, respectively. <sup>b</sup>Vibrationally hot bands are also observed at 1968 and 2035  $\text{cm}^{-1}$ . <sup>c</sup>Vibrational cooling. <sup>d</sup>Carbonyl of spectator metal center. <sup>e</sup>Shoulder.

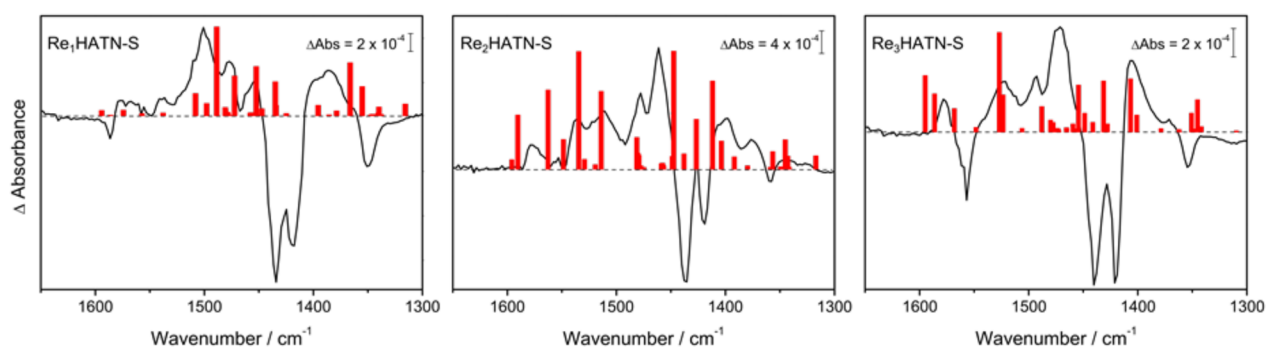
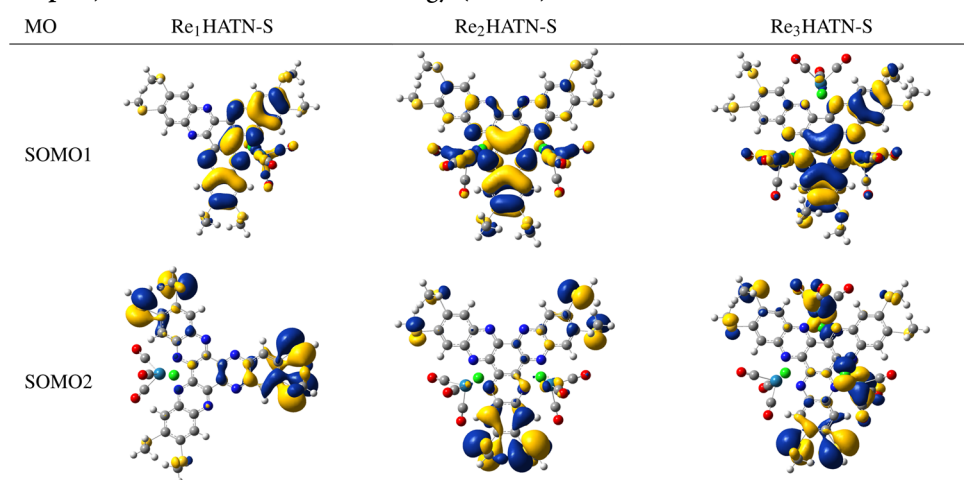


Figure 9. TRIR spectra of the HATN-S complexes in  $\text{CH}_2\text{Cl}_2$ , 100 ps after photolysis with a 400 nm pulse, acquired in the fingerprint region. The red bars indicate the oscillator strengths of calculated triplet state vibrational modes.

Table 6. Singly Occupied Molecular Orbitals (SOMOs) of the Triplet State Calculated with B3LYP, Where SOMO1 is the Higher Energy (Acceptor) and SOMO2 the Lower Energy (Donor)



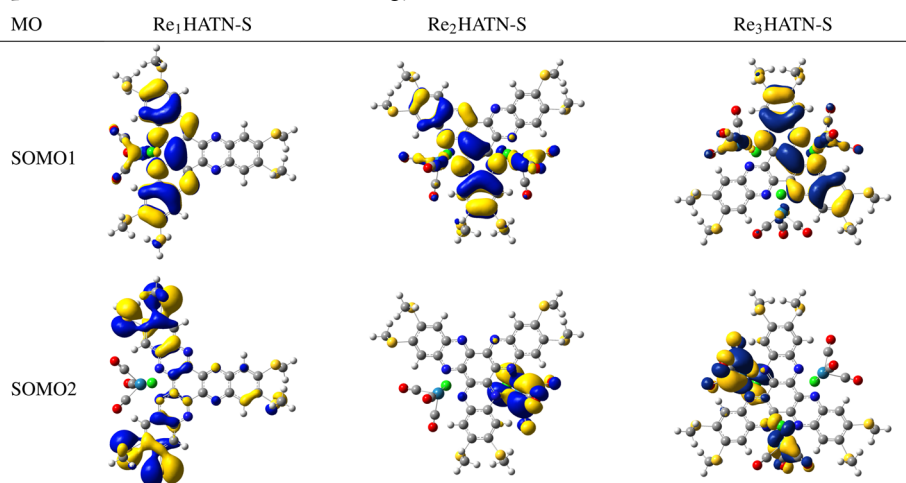
further discussed below. Unlike for the Re<sub>1</sub>HATN-S complex, there is no evidence for IL  $\pi,\pi^*$  states for Re<sub>2</sub>HATN-S and Re<sub>3</sub>HATN-S in TRIR spectra, and all MLCT excited state features return to the ground state. The magnitudes of the shifts in  $\nu(\text{CO})$  are again very low, with values of  $\Delta\nu$  approximately half of those observed for the HATN analogues.<sup>20</sup> The excited state lifetimes follow the trend Re<sub>1</sub>HATN-S > Re<sub>2</sub>HATN-S > Re<sub>3</sub>HATN-S, which is similar to previously observed results for HATN complexes,<sup>19</sup> Figure 8. This is consistent with the energy-gap law, according to which the excited state lifetime is inversely related to the difference between the ground and excited state energies.

TRIR spectra were also acquired in the fingerprint region, as shown in Figure 9, 100 ps after photolysis. The kinetics were found to be similar to the carbonyl region, and only peaks due

to one state are evident for each complex. A number of parent depletions are observed that match reasonably with the ground state FTIR spectra (see Table 5). Differences of ca. 6  $\text{cm}^{-1}$  can be observed for some depletions, which can be ascribed to partial overlap with excited state features as well as a strong  $\text{CH}_2\text{Cl}_2$  solvent band centered at 1423  $\text{cm}^{-1}$ . The excited state spectra show considerable differences based on the number of metals bound, indicating that the bonding of the HATN-S disk is significantly perturbed. In comparison, the differences in the ground state spectra are much less pronounced.

The nature of the excited states can be further investigated by considering the singly occupied MOs of the calculated triplet state. Compared to the frontier MOs from ground state calculations, a greater extent of contribution of the sulfur donors is predicted for Re<sub>2</sub>HATN-S and especially Re<sub>3</sub>HATN-

**Table 7. Singly Occupied Molecular Orbitals (SOMOs) of the Triplet State Calculated with CAM-B3LYP, Where SOMO1 is the Higher Energy (Acceptor) and SOMO2 the Lower Energy (Donor)**



S. Furthermore, the extent of delocalization of the orbital of the excited electron is decreased. This is consistent with the reduced red-shift of the  $\nu(1)$  vibrational mode for the HATN-S complexes when compared to analogous HATN complexes.<sup>19</sup> The change in delocalization due to the electron-withdrawing effects of additionally bound  $\{\text{Re}(\text{CO})_3\text{Cl}\}$  moieties can thus be said to be partially counteracted by the thioalkyl chains.

The lower energy calculated SOMO is the donor orbital, and the higher energy SOMO the acceptor. For Re<sub>1</sub>HATN-S, B3LYP calculations show the donor (SOMO2) to be sulfur-based and the acceptor (SOMO1) predominantly HATN-based (Table 6), so this may be described as an ILCT excited state. CAM-B3LYP calculations also show this, see Table 7. For Re<sub>2</sub>HATN-S, again B3LYP calculations show a sulfur-based donor MO and a predominantly HATN-based acceptor, suggesting an ILCT excited state. However, CAM-B3LYP calculations show a metal-based donor and the same HATN-based acceptor, which suggests an MLCT excited state. For Re<sub>3</sub>HATN-S, the lower energy donor SOMO has both sulfur and metal character, see Table 6, while the acceptor is predominantly HATN-based, which shows a mixed ILCT/MLCT excited state. CAM-B3LYP shows a donor orbital localized to two of the three metal centers, and a predominantly HATN-based acceptor, consistent with an MLCT triplet state. From this and TD-DFT calculations, it is clear that the functional used has a significant effect on the nature of the state calculated. Neither B3LYP nor CAM-B3LYP calculations are completely consistent with experimental data.

**Nanosecond Transient Absorption and Emission Spectroscopy.** HATN-S shows ground-state bleach in the region of 475 nm and above 400 nm. Transient absorption peaks are observed at 425 and 550 nm. Transient signals decay and bleaches recover with  $\tau$  of around 12  $\mu\text{s}$  in dichloromethane; this is attributed to a dark (nonemissive) state. Metal complexes exhibit subnanosecond decay of excited states, and as such detection is beyond the instrument limitation, but excited state lifetimes measured by TRIR are given in Table 5. The transient emission, with  $\lambda_{\text{max}}$  around 520 nm, has a lifetime convoluted with the laser pulse and therefore decays in less than 8 ns. Metal complexes did not show any detectable emission on this system.

## CONCLUSION

The ligand HATN-(SOct)<sub>6</sub> and the  $\{\text{Re}(\text{CO})_3\text{Cl}\}$  complexes thereof have been synthesized and isomers separated and assigned on the basis of previous work and  $R_f$  values. Electronic absorption spectra show transitions spanning the visible wavelengths, and these transitions are assigned as  $\pi, \pi^*$ , MLCT, ILCT, or MLCT/ILCT on the basis of TD-DFT calculations and resonance Raman spectroscopy. Time-resolved infrared spectroscopy is consistent with metal complexes showing a mixed MLCT/ILCT excited state, as carbonyl bands are shifted to higher frequency upon excitation, indicative of an MLCT state, but the shift is much smaller than analogous compounds which lack sulfur donors, indicating less donation from the metal, potentially due to donation from the sulfur groups.

## EXPERIMENTAL SECTION

**Materials.**  $\text{Re}(\text{CO})_5\text{Cl}$ , hexaketocyclohexane, 4,5-dichloro-1,2-phenylenediamine, and octane-1-thiol were used as received. HATN-(SOct)<sub>6</sub> was synthesized according to literature procedures.<sup>16</sup>

**$[\text{Re}(\text{CO})_3\text{Cl}(\text{HATN}(\text{SOct})_6)]$  (Re<sub>1</sub>HATN-S).** A total of 0.5 g (0.4 mmol) of HATN-(SOct)<sub>6</sub> and 0.145 g (0.4 mmol) of  $\text{Re}(\text{CO})_5\text{Cl}$  are refluxed in 0.15 L of ethanol overnight. The resulting dark-red solid is filtered. The crude solid is dissolved in the minimum amount of  $\text{CH}_2\text{Cl}_2$  and purified by column chromatography on silica gel (eluant  $\text{CH}_2\text{Cl}_2$ ). The band with an  $R_f$  of 0.85 is collected, and the solution is evaporated to dryness under vacuum to give a red solid. Yield = 0.364 g (0.22 mmol), 55%. <sup>1</sup>H NMR (400 MHz):  $\delta$  8.61 (s, 2H), 8.31 (s, 2H), 8.26 (s, 2H), 3.49 (m, 4H), 3.28 (m, 8H), 1.94 (m, 12H), 1.60 (m, 12H), 1.36 (m, 48H), 0.91 (t,  $J = 7$  Hz, 18H). Microanalysis calculated for  $\text{C}_{75}\text{H}_{108}\text{N}_6\text{O}_3\text{S}_6\text{ClRe}$ : C, 57.90; H, 7.00; N, 5.40. Found: C, 58.18; H, 7.26; N, 5.43. Low res MS (MALDI-TOF, TCNQ matrix) 1499.6 M – 2CO, calcd 1498.5.

***syn/anti*- $[(\text{Re}(\text{CO})_3\text{Cl})_2(\mu\text{-HATN}(\text{SOct})_6)]$  (Re<sub>2</sub>HATN-S).** A total of 0.2 g (0.16 mmol) of HATN-(SOct)<sub>6</sub> and 0.116 g (0.32 mmol) of  $\text{Re}(\text{CO})_5\text{Cl}$  are refluxed in 50 mL of toluene overnight. The resulting brown solution is evaporated under vacuum to dryness. The crude brown solid is dissolved in the minimum volume of  $\text{CH}_2\text{Cl}_2$ , and the two isomers were separated by column chromatography on silica gel (eluant  $\text{CH}_2\text{Cl}_2$ /pet. ether 5%). First major fraction  $R_f = 0.9$ , second major fraction  $R_f = 0.3$ . It was also common for small amounts of mono- and trinuclear products to form in the reaction.

Data for *anti*- $[(\text{Re}(\text{CO})_3\text{Cl})_2(\mu\text{-HATN}(\text{SOct})_6)]$  follow ( $R_f = 0.9$ ): yield = 0.104 g (0.056 mmol), 35%. <sup>1</sup>H NMR (400 MHz):  $\delta$  8.61 (s, 2H), 8.53 (s, 2H), 8.30 (s, 2H), 3.50 (m, 8H), 3.30 (t,  $J = 7$  Hz, 4H),

1.95 (m, 12H), 1.62 (m, 12H), 1.37 (m, 48H), 0.90 (m, 18H). Microanalysis calculated for  $C_{78}H_{108}N_6O_6S_6Cl_2Re_2$ ; C, 50.33; H, 5.85; N, 4.51. Found; C, 50.18; H, 5.95; N, 4.60. Low res MS (MALDI-TOF, TCNQ matrix)  $1776.5 = M - 3CO$ , calcd 1776.4.

Data for *syn*-[(Re(CO)<sub>3</sub>Cl)<sub>2</sub>(μ-HATN-(SOct)<sub>6</sub>)] follow ( $R_f = 0.3$ ): yield = 0.090 g (0.048 mmol), 30%. <sup>1</sup>H NMR (400 MHz): δ 8.69 (s, 2H), 8.60 (s, 2H), 8.30 (s, 2H), 3.50 (m, 8H), 3.30 (t,  $J = 7$  Hz, 4H), 1.95 (m, 12H), 1.62 (m, 12H), 1.37 (m, 48H), 0.90 (m, 18H). Microanalysis calculated for  $C_{78}H_{108}N_6O_6S_6Cl_2Re_2$ ; C, 50.33; H, 5.85; N, 4.51. Found: C, 50.29; H, 5.88; N, 4.55. Low res MS (MALDI-TOF, TCNQ matrix)  $1776.5 = M - 3CO$  calcd 1776.4.

*syn/anti*-[(Re(CO)<sub>3</sub>Cl)<sub>3</sub>(μ-HATN-(SOct)<sub>6</sub>)] (**Re<sub>3</sub>HATN-S**). A total of 0.15 g (0.12 mmol) of HATN-(SOct)<sub>6</sub> and 0.13 g (0.36 mmol) of Re(CO)<sub>3</sub>Cl are refluxed in 100 mL of chloroform overnight. The resulting purple solution is evaporated under vacuum to dryness. The crude purple solid is dissolved in the minimum volume of CH<sub>2</sub>Cl<sub>2</sub>, and the two isomers are separated by column chromatography on silica gel (eluant CH<sub>2</sub>Cl<sub>2</sub>). First major fraction  $R_f = 0.95$ , second major fraction  $R_f = 0.2$ . It was also common for small amounts of binuclear products to form in the reaction. Data for *anti*-[(Re(CO)<sub>3</sub>Cl)<sub>3</sub>(μ-HATN-(SOct)<sub>6</sub>)] follow ( $R_f = 0.95$ ): yield = 0.083 g (0.038 mmol), 32%. <sup>1</sup>H NMR (400 MHz): δ 8.63 (s, 2H), 8.62 (s, 2H), 8.55 (s, 2H), 3.53 (m, 12H), 1.98 (m, 12H), 1.63 (m, 12H), 1.38 (m, 48H), 0.90 (t,  $J = 7$  Hz, 18H). Microanalysis calculated for  $C_{81}H_{108}N_6O_9S_6Cl_3Re_3$ ; C, 44.89; H, 5.02; N, 3.88. Found; C, 45.17; H, 5.07; N, 4.00. Low res MS (MALDI-TOF, TCNQ matrix)  $2082.4 = M - 3CO$  calcd 2082.4. Data for *syn*-[(Re(CO)<sub>3</sub>Cl)<sub>3</sub>(μ-HATN-(SOct)<sub>6</sub>)] follow ( $R_f = 0.2$ ): yield = 0.098 g (0.045 mmol), 37%. <sup>1</sup>H NMR (400 MHz): δ 8.71 (s, 6H), 3.53 (m, 12H), 1.98 (m, 12H), 1.63 (m, 12H), 1.38 (m, 48H), 0.90 (t,  $J = 7$  Hz, 18H). Microanalysis calculated for  $C_{81}H_{108}N_6O_9S_6Cl_3Re_3$ ; C, 44.89; H, 5.02; N, 3.88. Found; C, 44.66; H, 4.80; N, 3.91. Low res MS (MALDI-TOF, TCNQ matrix)  $2082.4 = M - 3CO$  calcd 2082.4.

**Physical Measurements.** Aldrich spectroscopic grade solvents were used for all spectroscopic measurements. Spectral data were analyzed using GRAMS/32 AI (Galactic Industries) software. Absorption spectra were measured on JASCO. <sup>1</sup>H NMR spectra were recorded on CDCl<sub>3</sub> solutions at room temperature at 400 MHz on a Varian 400MR spectrometer. Chemical shifts were internally referenced to the residual CHCl<sub>3</sub> peak at 7.26 ppm. Electrospray ionization high resolution mass spectra were recorded on a Bruker MicroTOF-Q mass spectrometer operating in positive mode. Analysis of elemental composition was made by the Campbell Microanalytical Laboratory at the University of Otago, Dunedin, New Zealand, using a Carlo Erba 1108 CHNS combustion analyzer. The estimated error in the measurements is ±0.3%. The electrochemical cell for cyclic voltammetry comprises a 1 mm diameter platinum rod working electrode embedded in a KefL-F cylinder with a platinum auxiliary electrode and a Ag/AgCl reference electrode. The potential of the cell was controlled by an EG&G PAR 273 A potentiostat with model 270 software. Solution concentrations were typically about 10 mM in CH<sub>2</sub>Cl<sub>2</sub> with 0.1 M tetrabutylammonium hexafluorophosphate (TBAPF<sub>6</sub>) added as a supporting electrolyte. Solutions were purged with N<sub>2</sub> for approximately 5 min prior to measurement. The scanning speed used was 0.1 V s<sup>-1</sup>. Cyclic voltammograms were calibrated against the decamethylferrocenium/decamethylferrocene (DMFc) couple (0.012 V in CH<sub>2</sub>Cl<sub>2</sub>)<sup>31</sup> and are reported relative to the saturated calomel electrode (SCE) for comparison with other data by subtracting 0.045 V.<sup>24</sup> FT-Raman spectra were collected on powder samples using a Bruker IFS-55 interferometer with a FRA/106S attachment. The excitation source was a Nd:YAG laser with an excitation wavelength of 1064 nm. Raman photons were detected with a liquid nitrogen-cooled D418T germanium diode. Spectra were measured with 196 scans, with laser power of 50 mW and spectra resolution of 4 cm<sup>-1</sup>. Resonance Raman spectra were recorded using a previously described setup.<sup>32–35</sup> Excitation wavelengths 350.7, 356.4, 406.7, 413.1, 568, and 647 nm were provided by a Krypton ion CW laser (Coherent Inc.); 457, 488, and 514 nm were provided by a CW argon ion laser (Coherent Inc.); and 448, 532, and 594 nm were provided by crystal diode lasers (CrystaLaser). Concentrations were typically 1 mM in dichloromethane. Transient absorption and

emission spectra were recorded on dichloromethane solutions with concentrations typically  $1 \times 10^{-5}$  M, which were degassed under argon for 10 min prior to measurement. Transients were acquired using a LP920 K TA system (Edinburgh Instruments), with excitation at 355 nm from pulsed third-harmonic radiation from a Brilliant (Quintel) Nd:YAG laser at 1 Hz, and a Xe900 450 W xenon arc lamp controlled by a XP920 pulser as the probe source in TA mode. Photons were dispersed using a TMS300-A Czerny–Turner monochromator with 1800 grooves mm<sup>-1</sup> grating, recorded on a R928 (Hamamatsu) photomultiplier and transcribed on a TDS3012C (Tektronix) digital oscilloscope. The change in optical density ( $\Delta OD$ ) is found from  $I_b/IT$  in which  $I_b$  is the intensity of transmitted light before the excitation pulse, and  $IT$  is the intensity of transmitted light after the excitation pulse.

TRIR spectra were recorded using the ULTRA instrument located at the Rutherford Appleton Laboratory. The data were recorded using time-resolved multiple probe spectroscopy (TR<sup>MPS</sup>).<sup>36,37</sup> Briefly, two Ti:sapphire amplifiers, 10 kHz and 1 kHz, are synchronized using a common 65 MHz oscillator. The 1 kHz output is used as a pump, and the 10 kHz is used as the probe, to permit a pump–probe–probe–probe... data recording scheme. The 400 nm pump is generated by frequency doubling the 1 kHz fundamental output while the mid-IR probe is generated using an optical parametric amplifier with a difference frequency mixing unit (both Light Conversion). The pump–probe time delay is controlled up to 100 μs using a combination of electronic and optical delay. Each pump pulse is followed by 10 probe pulses each separated by 100 μs. Full details of the TRIR setup have been provided in ref 34. The power of the pump pulse is monitored before each experiment and set using a neutral density filter. A fraction of the probe pulse is dispersed onto an MCT detector to serve as the reference while the remainder was passed through the sample, dispersed by two grating monochromators and detected by two 128-channel linear MCT array detectors. Each monochromator is tuned to a different spectral region with a small overlap to obtain the largest bandwidth. Samples were circulated in a closed flow system attached to a Harrick solution cell with CaF<sub>2</sub> windows, spaced by 400 μm with Teflon spacers. The sample cell was rastered in the two dimensions orthogonal to the direction of beam propagation in order to minimize sample breakdown and localized heating.

## COMPUTATIONAL METHODS

Density functional theory using the Gaussian09 program suite<sup>38</sup> was used for calculations on these compounds. The B3LYP and CAM-B3LYP functionals were employed for *in vacuo* optimizations and calculations of vibrational frequencies. Electronic transitions were predicted using time-dependent DFT (TD-DFT) both *in vacuo* and using the IEFPCM (integral equation formalism polarizable continuum model) solvent model with dichloromethane, using the B3LYP and CAM-B3LYP functionals on their, respectively, optimized structures. Mulliken charge analysis was carried out from calculations that included the solvent model and utilized either the B3LYP or CAM-B3LYP functional. In all calculations, the LANL2DZ effective core potential was used to model rhenium atoms, as this has been shown to be suitable in many related systems, while the remaining atoms were modeled using a 6-31G(d) basis set. SOct groups were modeled as SMe groups to reduce computational expense, as this is not expected to affect any calculated properties. Calculated vibrational energies (cm<sup>-1</sup>) were scaled as to minimize the mean absolute deviation between experimental and calculated values; scale factors were generally around 0.975. Calculated Raman activities ( $S_j$ ) were converted to Raman intensities at 1064 nm using the following equation.<sup>39</sup>

$$\frac{\partial \sigma_j}{\partial \Omega} = \left( \frac{2^4 \pi^4}{45} \right) \left( \frac{(v_0 - \nu_j)^4}{1 - \exp\left[\frac{-h\nu_j}{kT}\right]} \right) \left( \frac{h}{8\pi^2 c \nu_j} \right) S_j$$

Molecular orbitals were visualized using Gaussview (Gaussian Inc.), and vibrational modes were illustrated using Molden.<sup>40</sup>

## ■ ASSOCIATED CONTENT

### ■ Supporting Information

Mulliken charge analysis of TD-DFT predicted transitions with B3LYP and CAM-B3LYP functionals; Cartesian coordinates for optimized HATN-S singlet, Re<sub>1</sub>HATN-S singlet, Re<sub>1</sub>HATN-S triplet, Re<sub>2</sub>HATN-S singlet, Re<sub>2</sub>HATN-S triplet, Re<sub>3</sub>HATN-S singlet, Re<sub>3</sub>HATN-S triplet, all with B3LYP and CAM-B3LYP functionals; ns-TA spectrum of HATN-S. This material is available free of charge via the Internet at <http://pubs.acs.org>.

## ■ AUTHOR INFORMATION

### Corresponding Authors

\*E-mail: [mike.george@nottingham.ac.uk](mailto:mike.george@nottingham.ac.uk)

\*E-mail: [kgordon@chemistry.otago.ac.nz](mailto:kgordon@chemistry.otago.ac.nz)

### Notes

The authors declare no competing financial interest.

## ■ REFERENCES

- (1) Caspar, J. V.; Meyer, T. J. *J. Phys. Chem.* **1983**, *87*, 952–957.
- (2) Caspar, J. V.; Westmoreland, T. D.; Allen, G. H.; Bradley, P. G.; Meyer, T. J.; Woodruff, W. H. *J. Am. Chem. Soc.* **1984**, *106*, 3492–3500.
- (3) Sato, S.; Matubara, Y.; Koike, K.; Falkenstrom, M.; Katayama, T.; Ishibashi, Y.; Miyasaka, H.; Taniguchi, S.; Chosrowjan, H.; Mataga, N.; Fukazawa, N.; Koshihara, S.; Onda, K.; Ishitani, O. *Chem.—Eur. J.* **2012**, *18*, 15722–15734.
- (4) Zalis, S.; Consani, C.; Nahhas, A. E.; Cannizzo, A.; Chergui, M.; Hartl, F.; Vlček, A., Jr. *Inorg. Chim. Acta* **2011**, *374*, 578–585.
- (5) Yi, X.; Zhao, J.; Sun, J.; Guo, S.; Zhang, H. *Dalton Trans.* **2013**, *42*, 2062–2074.
- (6) Portenkirchner, E.; Oppelt, K.; Ulbricht, C.; Egbe, D. A.; Neugebauer, H.; Knör, G.; Sariciftci, N. S. *J. Organomet. Chem.* **2012**, *716*, 19–25.
- (7) Bian, Z.-Y.; Wang, H.; Fu, W.-F.; Li, L.; Ding, A.-Z. *Polyhedron* **2012**, *32*, 78–85.
- (8) Koike, K.; Naito, S.; Sato, S.; Tamaki, Y.; Ishitani, O. *J. Photochem. Photobiol., A* **2009**, *207*, 109–114.
- (9) Bian, Z.-Y.; Sumi, K.; Furue, M.; Sato, S.; Koike, K.; Ishitani, O. *Inorg. Chem.* **2008**, *47*, 10801–10803.
- (10) Gholamkhash, B.; Mametsuka, H.; Koike, K.; Tanabe, T.; Furue, M.; Ishitani, O. *Inorg. Chem.* **2005**, *44*, 2326–2336.
- (11) Benson, E. E.; Sampson, M. D.; Grice, K. A.; Smieja, J. M.; Froehlich, J. D.; Friebel, D.; Keith, J. A.; Carter, E. A.; Nilsson, A.; Kubiak, C. P. *Angew. Chem., Int. Ed.* **2013**, *52*, 4841–4844.
- (12) Kurz, P.; Probst, B.; Spingler, B.; Alberto, R. *Eur. J. Inorg. Chem.* **2006**, *15*, 2966–2974.
- (13) Zhao, F.; Qu Liu, W.; Ying Xia, H.; Bo Wang, Y. *Comput. Theor. Chem.* **2012**, *997*, 49–54.
- (14) Kaafarani, B. R.; Kondo, T.; Yu, J.; Zhang, Q.; Dattilo, D.; Risko, C.; Jones, S. C.; Barlow, S.; Domercq, B.; Amy, F.; Kahn, A.; Bredas, J.-L.; Kippelen, B.; Marder, S. R. *J. Am. Chem. Soc.* **2005**, *127*, 16358–16359.
- (15) Barlow, S.; Zhang, Q.; Kaafarani, B. R.; Risko, C.; Amy, F.; Chan, C. K.; Domercq, B.; Starikova, Z. A.; Antipin, M. Y.; Timofeeva, T. V.; Kippelen, B.; Bredas, J.-L.; Kahn, A.; Marder, S. R. *Chem.—Eur. J.* **2007**, *13*, 3537–3547.
- (16) Kestemont, G.; de Halleux, V.; Lehmann, M.; Ivanov, D. A.; Watson, M.; Geerts, Y. H. *Chem. Commun.* **2001**, 2074–2075.
- (17) Crispin, X.; Cornil, J.; Friedlein, R.; Okudaira, K. K.; Lemaure, V.; Crispin, A.; Kestemont, G.; Lehmann, M.; Fahlman, M.; Lazzaroni, R.; Geerts, Y.; Wendin, G.; Ueno, N.; Brédas, J.-L.; Salaneck, W. R. *J. Am. Chem. Soc.* **2004**, *126*, 11889–11899.
- (18) Lehmann, M.; Kestemont, G.; Aspe, R. G.; Buess-Herman, C.; Koch, M. H. J.; Debije, M. G.; Piris, J.; de Haas, M. P.; Warman, J. M.; Watson, M. D.; Lemaure, V.; Cornil, J.; Geerts, Y. H.; Gearba, R.; Ivanov, D. A. *Chem.—Eur. J.* **2005**, *11*, 3349–3362.
- (19) Fraser, M. G.; Clark, C. A.; Horvath, R.; Lind, S. J.; Blackman, A. G.; Sun, X.-Z.; George, M. W.; Gordon, K. C. *Inorg. Chem.* **2011**, *50*, 6093–6106.
- (20) Fraser, M. G.; Blackman, A. G.; Irwin, G. I. S.; Easton, C. P.; Gordon, K. C. *Inorg. Chem.* **2010**, *49*, 5180–5189.
- (21) Fraser, M. G.; van der Salm, H.; Cameron, S. A.; Barnsley, J. E.; Gordon, K. C. *Polyhedron* **2013**, *52*, 623–633.
- (22) Jia, C.; Liu, S.-X.; Tanner, C.; Leiggenger, C.; Sanguinet, L.; Levillain, E.; Leutwyler, S.; Hauser, A.; Decurtins, S. *Chem. Commun.* **2006**, 1878–1880.
- (23) Liu, B.; Ran, Y.-F.; Li, Z.; Liu, S.-X.; Jia, C.; Decurtins, S.; Wandlowski, T. *Chem.—Eur. J.* **2010**, *16*, 5008–5012.
- (24) Bard, A. J.; Faulkner, L. R. *Electrochemical Methods*, 2nd ed.; John Wiley and Sons, Inc.: New York, 2001.
- (25) Kayanuma, M.; Daniel, C.; Gindensperger, E. *Can. J. Chem.* **2014**, *92*, 979–986.
- (26) Jacquemin, D.; Perpète, E. A.; Scuseria, G. E.; Ciofini, I.; Adamo, C. *J. Chem. Theory Comput.* **2008**, *4*, 123–135.
- (27) Yanai, T.; Tew, D. P.; Handy, N. C. *Chem. Phys. Lett.* **2004**, *393*, 51–57.
- (28) Guthmüller, J.; Gonzalez, L. *Phys. Chem. Chem. Phys.* **2010**, *12*, 14812–14821.
- (29) Butler, J. M.; George, M. W.; Schoonover, J. R.; Dattelbaum, D. M.; Meyer, T. J. *Coord. Chem. Rev.* **2007**, *251*, 492.
- (30) Bredenbeck, J.; Helbing, J.; Hamm, P. *J. Am. Chem. Soc.* **2004**, *126*, 990.
- (31) Noviandri, I.; Brown, K. N.; Fleming, D. S.; Gulyas, P. T.; Lay, P. A.; Masters, A. F.; Phillips, L. J. *Phys. Chem. B* **1999**, *103*, 6713–6722.
- (32) Howell, S. L.; Gordon, K. C. *J. Phys. Chem. A* **2004**, *108*, 2536–2544.
- (33) Lind, S. J.; Gordon, K. C.; Waterland, M. R. *J. Raman Spectrosc.* **2008**, *39*, 1556–1567.
- (34) Lind, S. J.; Walsh, T. J.; Blackman, A. G.; Polson, M. I. J.; Irwin, G. I. S.; Gordon, K. C. *J. Phys. Chem. A* **2009**, *113*, 3566–3575.
- (35) Horvath, R.; Fraser, M. G.; Cameron, S. A.; Blackman, A. G.; Wagner, P.; Officer, D. L.; Gordon, K. C. *Inorg. Chem.* **2013**, *52*, 1304–1317.
- (36) Greetham, G. M.; Burgos, P.; Cao, Q.; Clark, I. P.; Codd, P. S.; Farrow, R. C.; George, M. W.; Kogimtzis, M.; Matousek, P.; Parker, A. W.; Pollard, M. R.; Robinson, D. A.; Xin, Z. J.; Towrie, M. *Appl. Spectrosc.* **2010**, *64*, 1311–1309.
- (37) Greetham, G. M.; Sole, D.; Clark, I. P.; Parker, A. W.; Pollard, M. R.; Towrie, M. *Rev. Sci. Instrum.* **2012**, *83*, 103107.
- (38) Frisch, M. J.; et al. *Gaussian 09 Revision A.02*; Gaussian Inc.: Wallingford, CT, 2009.
- (39) Horvath, R.; Gordon, K. C. *Coord. Chem. Rev.* **2010**, *254*, 2505–2518.
- (40) Schaftenaar, G.; Noordik, J. *J. Comput.-Aided Mol. Des.* **2000**, *14*, 123–134.